Environmental Science and Pollution Research (2019) 26:17321–17332
https://doi.org/10.1007/s11356-019-05081-6

RESEARCH ARTICLE

Adsorption, recovery, and regeneration of Cd by magnetic phosphate nanoparticles

Yujiao Li [1,2,3] · Zhimin Yang [1,2,3] · Yucheng Chen [1,2,3] · Lei Huang [1,2,3]

Received: 30 November 2018 / Accepted: 3 April 2019 / Published online: 23 April 2019

Abstract

Adsorption plays an important role in removing cadmium (Cd^{2+}) from water, and magnetic adsorbents are increasingly being used due to their ease of separation and recovery. Magnetic Fe_3O_4–coated hydroxyapatite (HAP) nanoparticles (nHAP-Fe_3O_4) were developed by co-precipitation and then used for the removal of Cd^{2+} from water. The properties of these nanoparticles were characterized by transmission electron microscopy, X-ray diffraction, Fourier transform infrared spectroscopy, and magnetization curves. Experiments were conducted to investigate the effects of adsorption and mechanisms. Results illustrated that kinetic data were well fitted by a pseudo-second-order model. The adsorption capacity of nHAP-Fe_3O_4 was 62.14 mg/g. The mechanisms for the adsorption of Cd^{2+} on nHAP-Fe_3O_4 included rapid surface adsorption, intraparticle diffusion, and internal particle bonding, with the ion exchange with Ca^{2+} and chemical complexation being the most dominant. The regeneration efficiency and recovery rate of nHAP-Fe_3O_4 eluted by EDTA-Na_2 after the fifth cycle were 63.04% and 40.2%, respectively. Results revealed that the feasibility of nHAP-Fe_3O_4 as an adsorbent of Cd^{2+} and its environmental friendliness make it an ideal focus for future research.

Keywords Magnetic · Hydroxyapatite · Water treatment · Cadmium · Adsorption

Introduction

With the development of industry and mining, metallurgy, electroplating, printing, and dye manufacturing, cadmium (Cd^{2+}), as a potential heavy metal pollutant, contaminates water bodies (Qian 2007; Yang et al. 2016a) and thus harms plants, animals, and human health because of its difficult removal in the environment (Heitmann et al. 2014). Cd^{2+} is a heavy metal with high mobility, and it easily causes a series of hazards when it is enriched in living organisms (Dey et al. 2016). Cd^{2+} becomes selectively enriched in organs such as the kidney and liver after entering human or animal bodies through the digestive and respiratory tracts, ultimately affecting normal metabolic activities and causing chronic Cd^{2+} poisoning (Ke et al. 2015). Unlike organic pollutants, heavy metals are often difficult to degrade under natural conditions after entering water bodies, and they possess strong migration properties (Wan et al. 2016; Rahmanian et al. 2018). Therefore, the removal of Cd^{2+} has become an important part of the current research. Some techniques, including chemical precipitation, ion exchange, and adsorption (Cheng et al. 2014), are used to remove Cd^{2+} from wastewater. Among these methods, adsorption is widely used due to its simple operation and economic advantages. The research on Cd^{2+} adsorption materials in wastewater is mainly focused on carbon materials (Ling et al. 2017; Liang et al. 2014), iron manganese oxides (Karami 2013; Khraisheh et al. 2004), nanoferromagnetic materials (Su et al. 2014; Zendehdel et al. 2018), clay minerals (Abollino et al. 2003; Basualto et al. 2017), biomass materials (Schiewer and Patil 2008; Ajmal et al. 2003) and their modifications, and composite materials.

Responsible editor: Tito Roberto Cadaval Jr

✉ Yujiao Li
1170742896@qq.com

✉ Zhimin Yang
jerrioy@163.com; bear@swu.edu.cn

✉ Yucheng Chen
chenyucheng@swu.edu.cn

✉ Lei Huang
panda11@126.com

[1] Key Laboratory of the Three Gorges Reservoir Region's Eco-Environment (Ministry of Education), College of Resource and Environment, Southwest University, No. 2 Tiansheng Road Beibei, Chongqing 400715, People's Republic of China

[2] Chongqing Engineering Research Center of Rural Cleaning, Chongqing 400716, People's Republic of China

[3] Chongqing Key Laboratory of Agricultural Resources and Environment, Chongqing 400716, People's Republic of China

Apatite mineral has been widely studied because of its low cost and its reaction with a variety of metals to form heavy metal phosphates. As an apatite mineral, hydroxyapatite (HAP) is an important component of human teeth and bones, and it has good biological activity and biocompatibility. The special crystal structure of HAP makes it effective in ion exchange and in the removal of heavy metal ions from wastewater (Yamamura et al. 2018). Nano-hydroxyapatite (nHAP) has a small particle size and a large specific surface area and thus has a stronger adsorption capacity than ordinary apatite; as a result, it has attracted much attention in recent years (Guo et al. 2017). Yang et al. (2016b) prepared HAP with poor crystallinity for adsorbing copper in solutions. Guo et al. (2018) prepared an attapulgite HAP composite via a co-precipitation method with attapulgite as the matrix. They found that the maximum adsorption capacity of Cd^{2+} in the solution can reach 1.99 mmol/g. A hydroxyapatite/calcium silicate hydrate prepared by a phosphate recovery method was performed by Zhang et al. (2018b). They found that calcium silicate hydrate and hydroxyapatite/calcium silicate hydrate were effective for heavy metal retention but that the adsorption capacity of the latter was greater due to the presence of phosphate. However, these adsorbents used in existing studies are inconvenient to separate.

Magnetic nanoparticles have attracted considerable interest in the research on environmental remediation due to their large surface area, easy separation, and convenient recovery. Bare magnetite nanoparticles are likely oxidized in air, and the stability of the magnetite in the environment can be increased by modifications on its surface. For example, a calcium-based magnetic biomass carbon was prepared by biochar and magnetic materials and then used to adsorb Cd^{2+} in an aqueous solution; the adsorption amounts were 6.34 and 10.07 mg/g (Wu et al. 2018), respectively. Humic acid–coated magnetite nanoparticles have also been used as adsorbents to remove heavy metals, such as copper (Cu), Cd^{2+}, and mercury (Liu et al. 2015). Phosphate, a natural environmentally friendly material, can be combined with magnetite to increase its stability. In addition, recent research has indicated that phosphate can form insoluble salts with various heavy metals and that it is widely used in environmental restoration (Beesley and Marmiroli 2011; Bachoua et al. 2016).

In this study, a nanomagnetic HAP (nHAP-Fe_3O_4) prepared by co-precipitation (Zhuzhou 2007) with hydroxyapatite, iron salt, and ferrous salt was developed for the adsorption and removal of Cd^{2+} from the water. The physical and chemical characterization of nHAP-Fe_3O_4 were investigated, and the removal effect and mechanism of Cd^{2+} by nHAP-Fe_3O_4 in the solution were studied to provide a scientific basis for the repair of Cd^{2+} in magnetic composite materials.

Materials and method

Materials and preparation of nHAP-Fe_3O_4

The nHAP (particle size 60 nm), $FeCl_2{\cdot}4H_2O$, $FeCl_3{\cdot}6H_2O$, $CdCl_2{\cdot}2.5H_2O$, and ammonium water used were all of the analytical grade.

The bare and nHAP-coated Fe_3O_4 magnetic nanoparticles were prepared by co-precipitation. Briefly, 1.020 g of $FeCl_2{\cdot}4H_2O$ was dissolved in 50 mL of pure water and then added into 100 mL of pure water containing 2.770 g of $FeCl_3{\cdot}6H_2O$ under vigorous mechanical stirring. Then, the solution was heated to 80 °C, and ammonium water was added until its pH reached approximately 8. The black precipitate produced instantly was the Fe_3O_4 nanoparticle. A certain amount of nHAP was ultrasonically dispersed in pure water and was then added to the newly prepared Fe_3O_4 solution after heating to 80 °C. The solution was stirred continuously for 2 h, and the whole reaction temperature was controlled at 75 ± 5 °C under N_2 protection. The precipitate was then separated using a magnet after the reaction and washed with ethanol and pure water to neutral pH. The obtained product was nHAP-Fe_3O_4, which was then freeze-dried and ground for use.

Characterization of nanoparticles

The crystalline structures of the bare and nHAP-Fe_3O_4 magnetic nanoparticles were characterized by X-ray powder diffraction (BRUKER D8 ADVANCE, Germany), operated on Co Kα radiation, with a 2θ scan range from 10 to 90° and a rate of 6°/min. The infrared spectrometer (Nicolet IS10, USA) was used to obtain the functional group of the material, and KBr was used for compression. A transmission electron microscope (TEM) (JEM-1200EX, Japan) was used to investigate the morphological structure of the material, and TEM images were obtained using 120 kV acceleration voltage. The samples were prepared by dispersing a certain number of particles in deionized water with an ultrasonic bath. Then, a few drops of the suspended liquid were transferred to a 400-mesh Cu grid. After the instrument ran automatically for 40 min, the Cu mesh with samples was inserted into the sample chamber to observe the sample morphology. The magnetic properties of the samples were recorded using the liquid-free multifunction vibrating sample magnetometer system (Versalab, Quantum, USA). Analysis was performed using X-ray photoelectron spectroscopy (XPS, Thermo Escalab 250Xi, USA), and the spectra were collected with monochrome Al Ka (hv = 1486.6 eV) operated at 150 W and 650-μm beam spot. Charge correction was done with contaminated carbon C1s = 284.8 eV.s.

Table 1 Basic physicochemical properties of nanoparticles in this study

	Particle size (nm)	pH	Surface area (m^2/g)	nHAP:Fe_3O_4	Isoelectric point	Saturation magnetization (emu/g)
Fe_3O_4	5–25	7.03	94.5644	0:1	6.03	68.1
nHAP	60	7.95	70.3323	1:0	6.09	0
nHAP-Fe_3O_4	35	6.91	94.3944	1.14:1	3.08	34.1

Adsorption and regeneration experiment

In a typical adsorption procedure, 1000 mg/L $CdCl_2$ is prepared for use. In this study, 0.100 g of the as-prepared nanoparticles was then added into 50 mL of the mixed solution containing varying initial concentrations of Cd^{2+}. The shaking time was 1–1440 min. The pH of the mixture was adjusted to different values using HCl and NaOH. Then, the mixture was stirred for a certain time at 200 r/min and 25 °C. Thereafter, the magnetic nanoparticles with adsorbed heavy metals were separated from the mixture using a permanent handheld magnet. The amount of adsorbed Cd^{2+} was measured with an atomic absorption spectrophotometer. The adsorption capacity of the nanoparticles was determined using the following formula:

$$Q\mathrm{e} = \frac{(C_0 - C_t) \times \mathrm{V}}{m} \quad (1)$$

where Q_e (mg/g) is the amount of Cd^{2+} adsorbed at equilibrium; C_0 (mg/L) and C_t (mg/L) are the initial concentration and equilibrium concentration of the mixed solution, respectively; V (mL) is the volume of the solution, and m (mg) is the mass of the adsorbent. All experiments were repeated thrice, and the average results were reported.

Real wastewater features a complex composition, which may interfere with the adsorption performance of nHAP-Fe_3O_4. The effects of coexisting cations were studied using Na^+, Mg^{2+}, and Cu^{2+} as model cations by adding NaCl, $MgCl_2$, and $CuCl_2$. The ionic strength levels were set to 0, 20, 40, and 80 meq/L, with the concentration of Cd^{2+} set at 100 mg/L. Other conditions were the same as those in a typical adsorption procedure.

Table 2 Leaching of Fe, P, and Ca in different solutions of nHAP-Fe_3O_4

Water matrix	Fe (%)	P (%)	Ca (%)
Deionized water	NA	0.13	7.22
0.1 mol/L $CaCl_2$	NA	0.079	0.271
0.01 mol/L HCl	NA	43.63	50.41
0.1 mol/L HCl	7.87	44.54	51.37
0.5 mol/L HCl	85.92	100	100
1 mol/L HCl	91.83	100	100
5 mol/L HCl	100	100	100
2 mol/L NaOH	1.76	0.22	2.15

The recovery of the as-prepared nanoparticles was evaluated by regeneration processes using 0.01 mol/L HCl and 0.01 mol/L EDTA-Na_2, respectively. Briefly, 0.100 g of the as-prepared nanoparticles was added into 50 mL of the Cd^{2+} solution with a concentration of 250 mg/L. The resulting mixture was shaken for 3 h to reach the adsorption equilibrium. Then, the spent nanoparticles were eluted with 50 mL of 0.01 mol/L HCl and 0.01 mol/L EDTA-Na_2 for 3 h. After regeneration, the recovered materials were separated, washed with deionized water, and then used for the next adsorption experiments. The procedure was repeated for five consecutive cycles. The adsorption capacities of the nanoparticles were calculated by Formula (1).

The regeneration efficiency (%RE) of each cycle was calculated as follows (Ahmad et al. 2018):

$$\%\mathrm{RE} = \frac{Q_{e,i}}{Q_e} \times 100\% \quad (2)$$

where Q_e is the adsorption capacity of nHAP-Fe_3O_4. In addition, another 0.100 g of nanoparticles was subjected to the above procedure of adsorption and desorption, dried in a vacuum oven at 60 °C, and then weighed after each desorption. The recovery rate of adsorbent (%Ra) was calculated by the following formula:

$$\%\mathrm{Ra} = \frac{m_i}{m_0} \times 100\% \quad (3)$$

where m_i is the dry weight of adsorbent after each cycle and m_0 is the initial mass of the adsorbent.

Results and discussion

Basic properties

Through a pre-experiment, 1 g of Fe_3O_4 was found to load up to 1.14 g of nHAP, and the ratio of the raw materials of nHAP to Fe_3O_4 was 1:1. Therefore, this ratio was used in the successive tests. The basic physicochemical properties of the prepared materials are shown in Table 1. Nearly no free nanoparticles were observed in the solution through a magnetic separation after shaking, indicating that nHAP and Fe_3O_4 were tightly bound together and could not be separated by simple physical methods.

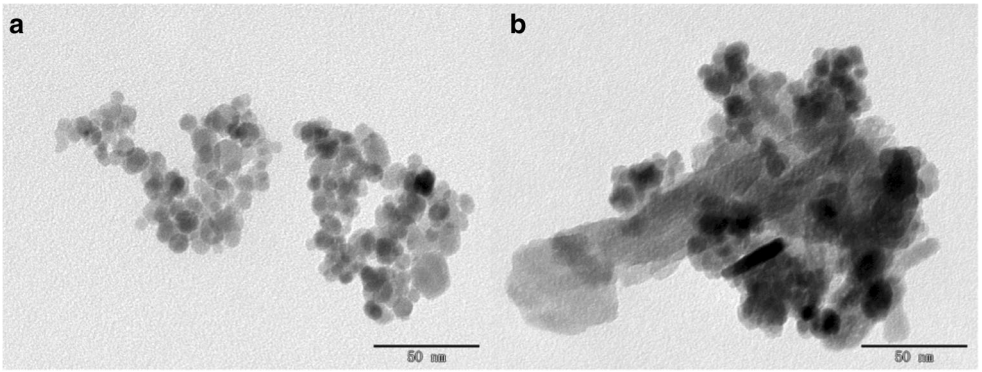

Fig. 1 TEM images of Fe_3O_4 **a** and nHAP-Fe_3O_4 **b**

The leaching of sorbent components into treated water is unfavorable to the environment. Deionized water; 0.1 mol/L $CaCl_2$; 0.01, 0.1, 0.5, 1, and 5 mol/L HCl; and 2 mol/L NaOH were used as the matrix to discuss the leaching property of the nanoparticles (Liu et al. 2015). Table 2 shows the leaching of Fe, P, and Ca in the different solutions of nHAP-Fe_3O_4. The nHAP-Fe_3O_4 dispersed by deionized water exhibited a free concentration of 0.13 mg/L phosphorus and nearly zero iron ions in equilibrium, whereas the concentration of free iron ions in the aqueous dispersion of Fe_3O_4 nanoparticles was 0.93 mg/L. This result indicated that the phosphate coating markedly improved the stability of the magnetic nanoparticles and reduced the release of nanomaterials into the environment. In the 0.01 and 0.1 mol/L HCl matrices, the leaching of Fe, P, and Ca from nHAP-Fe_3O_4 into the solution phase was below 10%, 45%, and 52%, respectively; when the concentration was increased to 0.5 mol/L, the leaching of Fe increased to 85.92%, and the phosphate was completely dissolved. The nHAP-Fe_3O_4 was completely leached out in 5 mol/L HCl. The leaching of Fe and P in pure water was found to be similar to that in 0.1 mol/L $CaCl_2$. This result indicated that the two solutions exerted similar effects on the stability of nHAP-Fe_3O_4. As the nanoparticles were prepared in basic solutions, the leaching values of Fe, P, and Ca in 2 mol/L NaOH was 1.76%, 0.22%, and 2.15%, respectively. Overall, the nHAP-Fe_3O_4 was stable in pure water, as well as in salt, weak acid, and basic solutions.

Characterization of Fe_3O_4 and nHAP-Fe_3O_4

Figure 1 shows the TEM images of the as-prepared Fe_3O_4 (a) and nHAP-Fe_3O_4 (b). The Fe_3O_4 magnetic nanoparticles (a) were spherical with typical sizes of 5–25 nm, and their distribution was relatively uniform. Figure 1 b shows the TEM images of the as-prepared nHAP-Fe_3O_4. nHAP was rod-shaped, typically 170 nm long and 35 nm thick, and had Fe_3O_4 attached on its surface. Similar observations were reported by Piar and Pakade (2015). Meanwhile, no obvious change was observed in the morphology and size of Fe_3O_4, and the combination of Fe_3O_4 caused the magnetic property of the as-prepared nanoparticles.

The results of the wide-angle X-ray diffraction are shown in Fig. 2. The broad peaks at diffraction angles of 35.1, 41.4, 50.5, 63.0, 67.4, and 74.3, which were characteristic of the

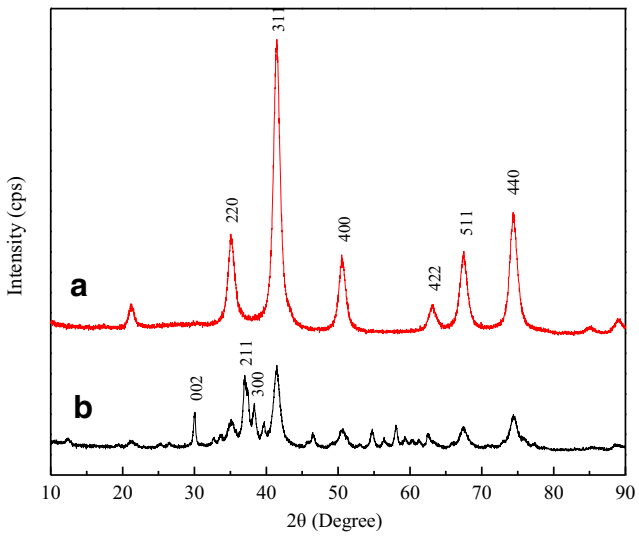

Fig. 2 X-ray diffraction of Fe_3O_4 **a** and nHAP-Fe_3O_4 **b**

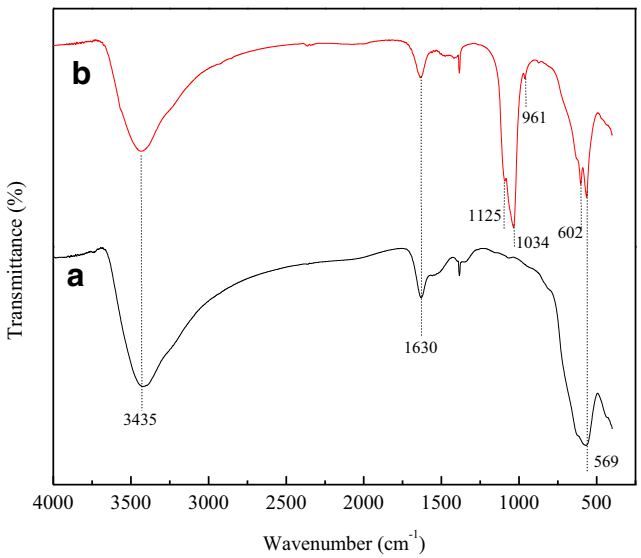

Fig. 3 IR Spectrum of Fe_3O_4 **a** and nHAP-Fe_3O_4 **b**

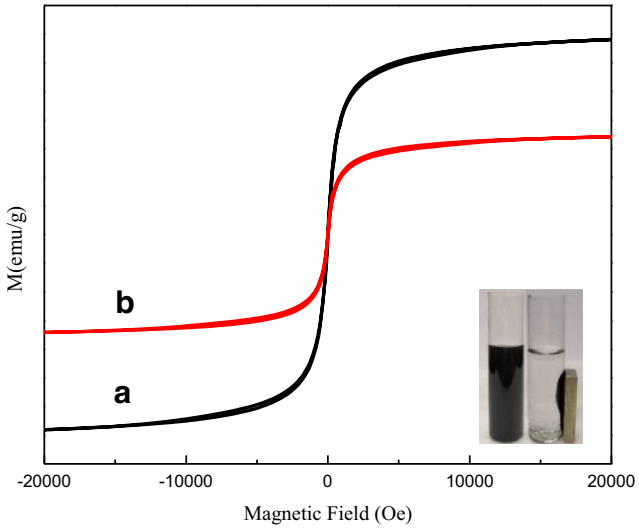

Fig. 4 Magnetization curves of Fe_3O_4 **a**, nHAP-Fe_3O_4 **b**, and its recover procedure

(220), (311), (400), (422), (511), and (440) crystal planes of the Jade PDF card (JCPDS 88-0315), respectively (Farokhi et al. 2018), were distinguished in the bare Fe_3O_4 and nHAP-Fe_3O_4. These peaks were of standard anti-spinel crystal form. The characteristic peaks of HAP (Fig. 2b) were noted at 37.0, 38.3, and 30.1, which corresponded to (JCPDS 72-1243) (211), (300), and (002) crystal planes (Núñez et al. 2014), respectively. Compared with that of the bare Fe_3O_4, the characteristic peak intensity of nHAP-Fe_3O_4 was significantly reduced, and no other diffraction peaks were observed, except for the peaks of Fe_3O_4 and HAP. This result indicated that no new substances were formed during the material synthesis. This finding also revealed that the combination of phosphate and Fe_3O_4 was mainly by electrostatic interaction and intermolecular force.

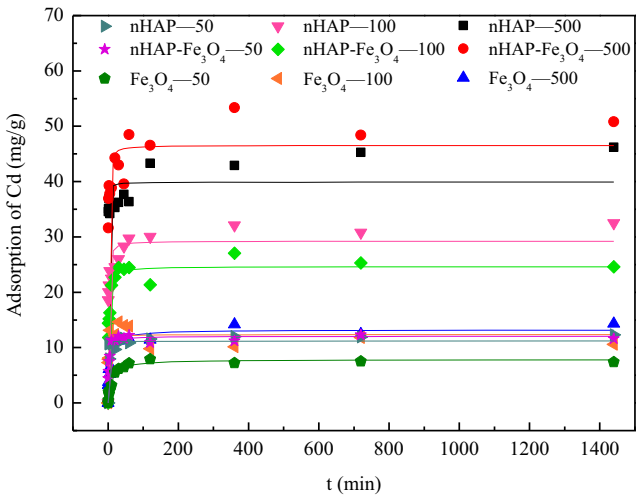

Fig. 5 Adsorption capacity of Cd^{2+} in 50, 100, and 500 mg/L by nHAP, nHAP-Fe_3O_4, and Fe_3O_4 at different times

Spectroscopic analysis showed that the nHAP was successfully coated on the surface of Fe_3O_4 (Fig. 3). The Fe–O stretch of nHAP-Fe_3O_4 was found at 569 cm^{-1} Ma et al. (2018b), and the absorption peaks at 3435 and 1630 cm^{-1} were attributed to the surface adsorption water (Viswanathan and Meenakshi 2008; Ahmad et al. 2019), as well as the hydroxyl stretching and bending vibration on the composite materials. The bands at 961 and 1034–1125 cm^{-1} were due to the PO_4^{3-} and P–O vibrations (Wei et al. 2017), and the band at 602 cm^{-1} was attributed to the characteristic peak of HAP (Nabavinia et al. 2019). Meanwhile, for the bare Fe_3O_4, no bands at 600–1200 cm^{-1} were observed, and the Fe–O vibration peak in the composite material was obviously weakened, also indicating the existence of nHAP on Fe_3O_4. For nHAP-Fe_3O_4, the peak at Fe–O was slightly offset in comparison with the case of the bare Fe_3O_4 most likely due to the influence of the nHAP.

Figure 4 shows the magnetization curves of Fe_3O_4 (a) and nHAP-Fe_3O_4 (b). No hysteresis effect was observed on the two materials, indicating that the materials prepared were super-paramagnetic. The saturation magnetizations were 68.1 and 34.1 emu/g for Fe_3O_4 and nHAP-Fe_3O_4, respectively. The saturation magnetization of nHAP-Fe_3O_4 decreased, indicating that nHAP was successfully coated on the surface of Fe_3O_4. A saturation value of 16.3 emu/g was reported to be sufficient for magnetic separation with a conventional magnet (Ma et al. 2005). In the solution test, the materials were completely separated from the solution by an external magnetic field.

Sorption study

Sorption kinetics

The sorption dynamics of Cd^{2+} to nHAP, nHAP-Fe_3O_4, and Fe_3O_4 were evaluated by adding 0.1 g of the as-obtained nanoparticles into 50 mL of a mixed solution containing 50, 100, and 500 mg/L Cd^{2+} at room temperature. The adsorption time was 1, 2, 3, 5, 10, 20, 30, 45, 60, 120, 360, 720, and 1440 min. The results are shown in Fig. 5. The adsorption capacities of the nanoparticles were determined with a quick step continuing up to 2 h, followed by a slow one up to the equilibrium state. The equilibrium adsorption capacities of nHAP, nHAP-Fe_3O_4, and Fe_3O_4 were 12.00, 11.20, and 7.20 mg/g at Cd^{2+} concentration of 50 mg/L; 32.10, 27.05, and 10.15 mg/g at Cd^{2+} concentration of 100 mg/L; and 46.20, 53.35, and 11.43 mg/g at Cd^{2+} concentration of 500 mg/L, respectively. The result indicated that the adsorption amount of nHAP was higher than that of the other two

Table 3 The kinetic model parameters for the adsorption of Cd^{2+} on nHAP, nHAP-Fe_3O_4, and Fe_3O_4 (C_0 50 mg/L, 100 mg/L, 500 mg/L)

Initial concentration (mg/L)		Pseudo-first-order model				Pseudo-second-order model				
		$Q_{e,exp}$ (mg/g)	$Q_{e,cal}$ (mg/g)	k_1 (min^{-1})	R^2	$Q_{e,cal}$ (mg/g)	k_2 (g/(mg min))	R^2	h (mg/(g min))	$t_{0.5}$ (min)
50	nHAP	12.00	10.93	3.8045	0.8658	11.18	0.5769	0.9021	72.15	0.15
	nHAP-Fe_3O_4	11.20	11.98	0.1470	0.9731	12.04	0.0456	0.9731	6.61	1.82
	Fe_3O_4	7.20	7.35	0.0662	0.9780	7.83	0.0127	0.9760	0.78	10.01
	nHAP	32.10	28.01	0.6957	0.8308	29.25	0.0373	0.9129	31.88	0.92
100	nHAP-Fe_3O_4	27.05	23.78	0.3716	0.8602	24.64	0.0259	0.9205	15.73	1.57
	Fe_3O_4	10.15	12.13	0.6069	0.7977	12.34	0.1060	0.7841	16.16	0.76
	nHAP	42.90	38.91	1.9902	0.8617	39.92	0.1031	0.9077	164.23	0.24
500	nHAP-Fe_3O_4	53.35	44.88	0.9935	0.8642	46.54	0.0366	0.9155	79.19	0.59
	Fe_3O_4	14.20	12.39	0.1186	0.8927	13.21	0.0132	0.9340	2.30	5.75

nanoparticles in a low concentration of Cd^{2+}. However, when the Cd^{2+} concentration was high, the adsorption of nHAP was lower than that of nHAP-Fe_3O_4.

The pseudo-first-order kinetic model (4) and pseudo-second-order kinetic model (5) were used to fit the adsorption data. The results are shown in Table 3. The data of nHAP and nHAP-Fe_3O_4 fitted the pseudo-second-order model well, with an excellent correlation coefficient of $R^2 > 0.9$, which implied the occurrence of chemisorption during the adsorption process (Ahmad et al. 2018). Meanwhile, the adsorption process of Fe_3O_4 could be described by the pseudo-first-order kinetic model with a correlation coefficient of 0.79–0.98. The above results indicated that the adsorption sites were mainly provided by the nHAP during the adsorption process. For the nHAP and nHAP-Fe_3O_4, the calculated h was large, and $t_{0.5}$ was small, indicating that the initial adsorption rate was fast and that the time to reach adsorption equilibrium was short. This finding is likely due to the large specific surface area that can provide many active binding sites for Cd^{2+}. Therefore, at the beginning of adsorption, Cd^{2+} was rapidly bound to the active sites on the surface due to the large concentration of Cd^{2+} in the solution while the adsorption rate gradually slowed down because of the decreasing number of active sites and Cd^{2+} concentration until equilibrium was reached (Zheng et al. 2010). Moreover, the theoretical equilibrium adsorption amount was equal to the practical value Ma et al. (2018a).

$$\ln(Q_e - Q_t) = \ln(Q_e) - k_1 t \tag{4}$$

$$\frac{t}{Q_t} = \frac{1}{Q_e} t + \frac{1}{k_2 Q_e^{\,2}} \tag{5}$$

where Q_e (mg/g) and Q_t (mg/g) are the amounts of Cd^{2+} adsorbed at equilibrium and at any time, respectively; and k_1 (min^{-1}) and k_2 (g/(mg·min)) are the rate constants of the pseudo-first-order kinetics and pseudo-second-order kinetics, respectively.

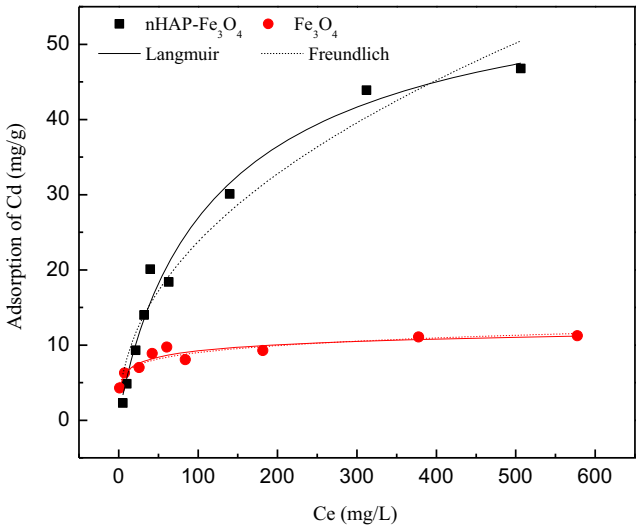

Fig. 6 Adsorption isotherm of Cd^{2+} by nHAP-Fe_3O_4 and Fe_3O_4

Adsorption isotherm

The adsorption capacity of the as-prepared nHAP-Fe_3O_4 to Cd^{2+} was measured at various initial concentrations (0, 10, 20, 40, 60, 80, 100, 200, 400, and 600 mg/L). The results (Fig. 6) showed that the adsorption capacity of Cd^{2+} increased with the increase of the equilibrium concentration within 24 h.

Table 4 Isotherm constants for Cd^{2+} adsorption on nHAP-Fe_3O_4 and Fe_3O_4

	The Langmuir			The Freundlich		
	Q_m (mg/g)	k	R^2	k_f	n	R^2
nHAP-Fe_3O_4	62.14	0.0127	0.9778	2.79	2.15	0.9529
Fe_3O_4	15.97	0.3393	0.8862	4.68	7.04	0.8849

Table 5 Adsorption of Cd^{2+} by different adsorbents

No.	Materials	Diameter	pH	Adsorption (mg/g)	Ref.
1	DPL	1 cm	–	18.26	Lee and Choi 2018
2	Mn_3O_4/Fe_3O_4	25–30 nm	7	13.6	Heitmann et al. 2014
3	$KBC_{mag-0.05}$	5–8 μm	–	33.89	Son et al. 2018
4	Fe_3O_4@$FePO_4$	10 nm	7	13.51	Zhang et al. 2018a
5	MNR	55–65 nm	5.5	88.39	Karami 2013
6	Fe_3O_4/HA	140 nm	6	50.4	Liu et al. 2015
7	Fe_3O_4/Mg–Al–CO_3–LDH	–	–	45.6	Shan et al. 2015
8	FeMnMg-LDH	–	–	59.99	Zhou et al. 2018
9	ACNF	–	–	0.960	Liang et al. 2016
10	PP biochars	–	5.0 ± 0.05	14.7	Zhang et al. 2017
11	nHAP-Fe_3O_4	5–25 nm	6.91	62.14	This study

The maximum adsorption capacities of the nHAP-Fe_3O_4 for Cd^{2+} were evaluated using the adsorption isotherms as follows:

$$Qe = \frac{k_1 Q_{max} C_e}{1 + k_1 C_e} \quad (6)$$

$$Qe = k_f C_e^{\frac{1}{n}} \quad (7)$$

where Q_e (mg/g) and Q_{max} (mg/g) represent the equilibrium adsorption capacity and maximum adsorption capacity of the nanoparticles, respectively; k_1 is the Langmuir constant related to the affinity of the adsorbent; C_e is the equilibrium concentration of Cd^{2+}; and k_f represents the Freundlich adsorption constant.

The isotherm parameters obtained from the models are listed in Table 4. The adsorption data fitted well with the Langmuir model, with the correlation coefficient (R^2) being 0.9778, which indicated that the adsorption process was a uniform adsorption of monolayers (Langmuir 1918). The adsorption capacity according to the Langmuir model was 62.14 mg/g, and the nHAP-Fe_3O_4 prepared in this study demonstrated a higher adsorption capacity for Cd^{2+} than did the materials reported in other studies (Table 5). The Freundlich fitting parameter $n > 1$ indicated that the adsorption of Cd^{2+} by nHAP-Fe_3O_4 was easy (Tang et al. 2018).

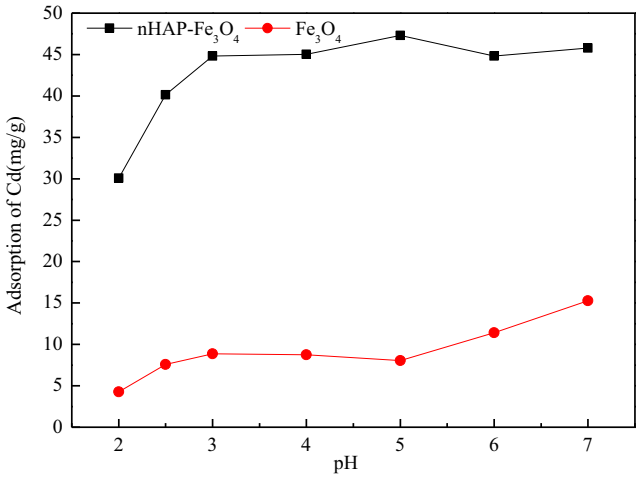

Fig. 7 The adsorption of Cd^{2+} by nHAP-Fe_3O_4 and Fe_3O_4 at different pH values

Effects of pH

The solution pH not only affects the Cd^{2+} adsorption capacity of nanoparticles but also adjusts the pH of the equilibrium liquid. It can also indirectly affect the adsorption of heavy metal ions by the material. The adsorption capacities of the nanoparticles for Cd^{2+} at pH values of 2, 2.5, 3, 4, 5, 6, and 7 in this study are shown in Fig. 7. The pH was found to greatly affect the adsorption of Cd^{2+}. The adsorption capacity of Cd^{2+} by the nHAP-Fe_3O_4 nanomaterials increased rapidly with the increase of pH from 2 to 3, and it became gentle with the increase of pH from 3 to 7. The pH of the zero charge point (pH_{PZC}) for nHAP-Fe_3O_4 was 3.08 (Table 1), which was obtained by plotting the charges at pH 2, 4, 6, 8, and 10. The charges were measured by a laser particle size analyzer (Zetasizer Nano ZS, Malvern, UK). Nanoparticles are negatively charged when $pH > pH_{PZC}$. Electrostatic attraction occurs with Cd^{2+}, which is positively charged, and as the pH increases, the zeta potential increases, and the adsorption capacity of Cd^{2+} becomes strong. In this study, the nHAP-Fe_3O_4

Table 6 The pH of equilibrium solution after treating 50 mL of water with 0.1 g nHAP-Fe_3O_4 and Fe_3O_4

pH	2	2.5	3	4	5	6	7
nHAP-Fe_3O_4	3.72	4.78	5.46	6.17	6.36	6.5	6.7
Fe_3O_4	3.03	4.57	4.86	5.22	5.78	6.20	6.83

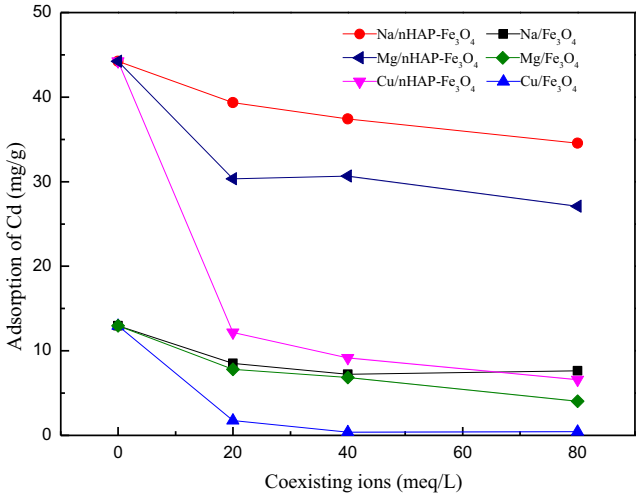

Fig. 8 The adsorption of Cd^{2+} by nHAP-Fe_3O_4 and Fe_3O_4 at different cation strengths

was positively charged when the pH of the material < pH_{PZC} while some Cd^{2+} became adsorbed. This result indicated the occurrence of other mechanisms, such as ion exchange and chelation reaction.

The charge on the surface of HAP was negative, thereby generating an electrostatic attraction with Cd^{2+} during the adsorption process. Cd^{2+} may gradually hydrolyze to $Cd(OH)_2$, $Cd(OH)_3^-$, and $Cd(OH)_4^{2-}$ during the gradual increase of pH acidity to alkalinity; this condition decreased the electrostatic attraction between the nanoparticles and Cd^{2+}, hence the slow increase in adsorption Zhang et al. (2018a).

The pH of the equilibrium solution is shown in Table 6. The pH of the solution increased when its pH was in the range of 2–6 but decreased when it was 7, which is close to 6.5. The solution pH values of 2.5 and 3 demonstrated the highest increase, indicating that the nanoparticles have a certain buffer capacity for the solution pH that can neutralize H^+ and OH^- in the solution.

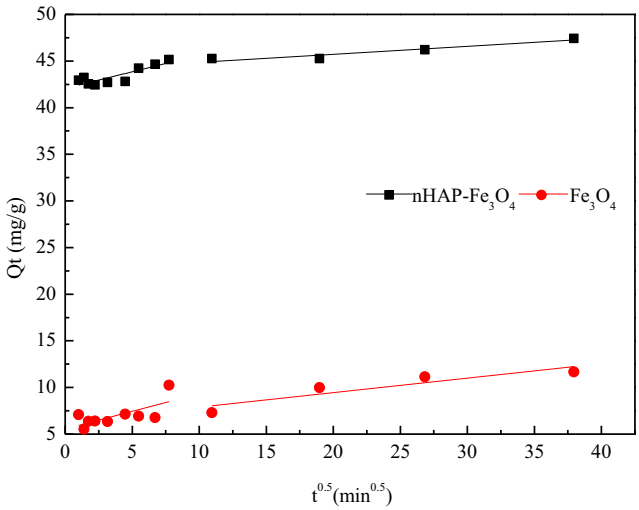

Fig. 9 Intraparticle diffusion curve for Cd^{2+} adsorption on nHAP-Fe_3O_4 and Fe_3O_4

Table 7 Intraparticle diffusion model constants and correlation coefficients for Cd^{2+} adsorption on nHAP-Fe_3O_4 and Fe_3O_4

	Intraparticle diffusion model					
	Kp_1	Kp_2	C_1	C_2	R_1^2	R_2^2
nHAP-Fe_3O_4	0.3545	0.0852	42.073	44.017	0.7431	0.9099
Fe_3O_4	0.3766	0.1562	5.558	6.321	0.4860	0.8445

Effects of coexisting cationics

The influence of commonly coexisting ions on the adsorption of Cd^{2+} was studied using Na^+, Mg^{2+}, and Cu^{2+} as model cations (Fig. 8). The results showed that obstacles occurred on the adsorption of Cd^{2+} in the existence of cations, and the adsorption capacity decreased with the increase of ionic strength, indicating that a competitive adsorption relationship existed between the cations and Cd^{2+}. The effects of the three ions on the adsorption process of Cd^{2+} were noted in the order $Cu^{2+} > Mg^{2+} > Na^+$, with a decreasing adsorption of Cd^{2+} from 44.24 mg/g to 6.59 mg/g. Even at low concentrations, the adsorption amount of Cd^{2+} was obviously decreased possibly because Cu^{2+} precipitated on the surface of the nanoparticles and some of the adsorption sites were masked (Qian 2007). Moreover, previous reports showed that the affinity of iron oxide and phosphate for heavy metals such as Cu^{2+} and Cd^{2+} is higher than that for Na^+ (Zhou et al. 2017). The radius of Na^+ is smaller than those of the other two cations, and therefore, the influence of Na^+ on Cd^{2+} adsorption is less obvious than that of $Mg^{2+}$and Cu^{2+}.

Adsorption mechanism

The above results showed that the adsorption mechanisms of heavy metal ions by magnetic hydroxyapatite might involve physical adsorption, ion exchange, and chemical complexation. To explore the internal factors affecting adsorption and the adsorption mechanism on nHAP-Fe_3O_4, we used the particle diffusion model and carried out XPS analysis. For many adsorptions, intraparticle diffusion is the control step of the adsorption rate, and the presence or absence of this process can be determined by the following formula:

$$Q_t = K_{Pi} t^{0.5} + C_i \quad (8)$$

where Kp_i (mg/(g $min^{0.5}$)) is the intraparticle diffusion rate constant; C_i is the boundary layer thickness, that is, serious particle diffusion blocking equates to a great boundary effect; and i represents the different adsorption stages.

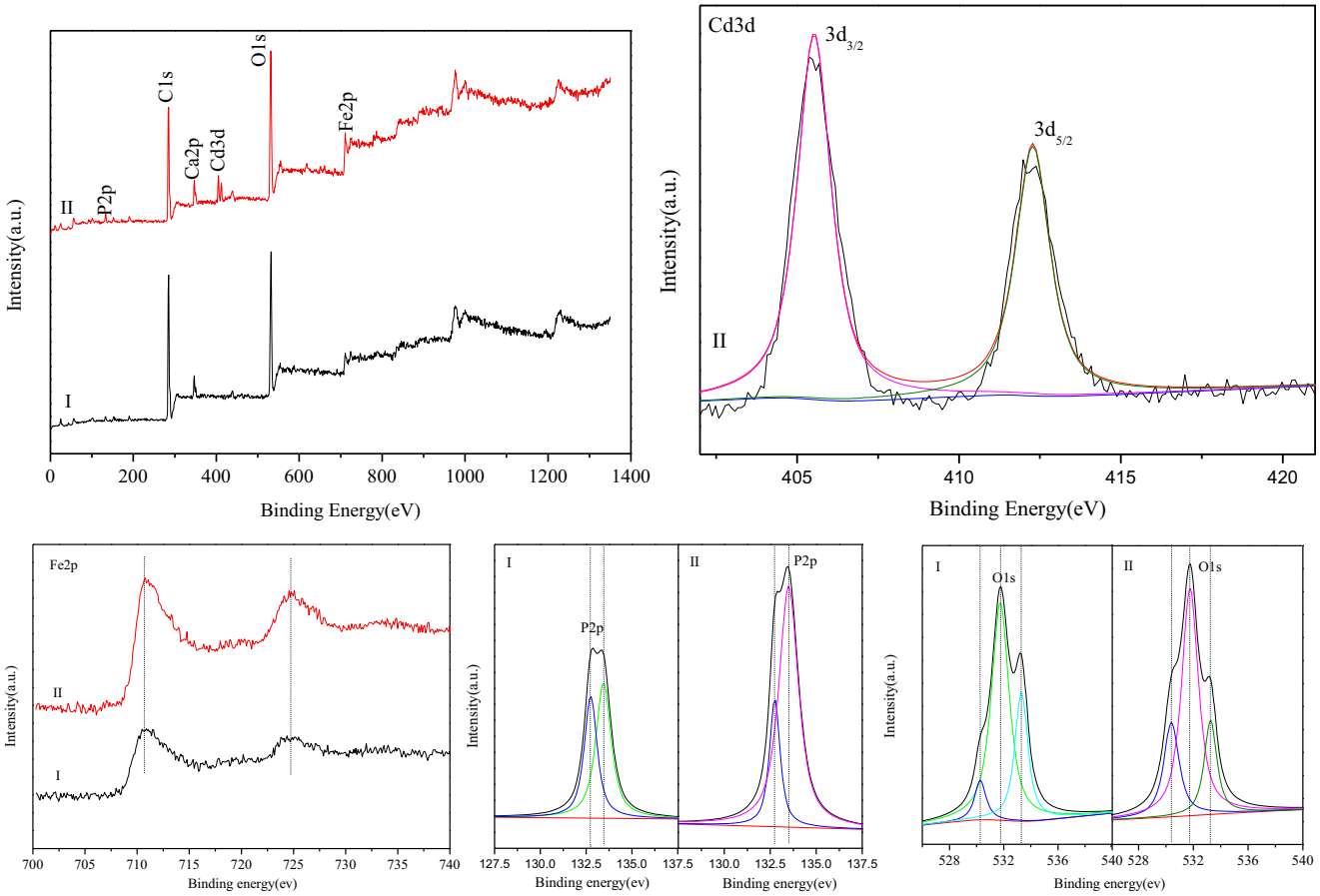

Fig. 10 XPS spectra of nHAP-Fe_3O_4 before (I) and after (II) adsorption with Cd^{2+}

The results with Q_t as the ordinate and $t^{0.5}$ as the abscissa are shown in Fig. 9. The fitting curve exhibited a multilevel linear relationship. The first stage is the initial stage of adsorption with a rapidly rising surface adsorption; the second stage continued for a long time, and the intraparticle diffusion served as the limiting step of the adsorption rate (Lei et al. 2018). The K_{p1} values of both materials were greater than K_{p2}, and C_2 was greater than C_1 (Table 7), indicating that at the beginning of the adsorption, the adsorption rate of Cd^{2+} was fast using the nanoparticles because of their large specific surface area. Then, as the adsorption progressed, the adsorption capacity of the particles gradually decreased. None of the fit curves passed through the origin, indicating that intraparticle diffusion was not the only step in controlling the adsorption rate (Adebisi et al. 2017).

The XPS analysis of nHAP-Fe_3O_4 before and after adsorption of Cd^{2+} is shown in Fig. 10. Compared with nHAP-Fe_3O_4 before adsorption, Cd^{2+} was present on the surface of the nHAP-Fe_3O_4 particles adsorbed by Cd^{2+}, and no change in chemical valence occurred. The peak shape and position of Fe2p before (curve I) and after (curve II) the reaction with Cd^{2+} demonstrated virtually no change; however, the intensity was changed, indicating that a strong relationship existed between Fe and Cd^{2+} and the formation of complexes (Chen et al. 2017). The peak shape of P2p at 133.5 eV after the reaction with Cd^{2+} was significantly enhanced, indicating that part of the phosphate participated in Cd^{2+} adsorption by forming complexes or via chemical bonding (Guivar et al. 2016). The analysis of O^{2-} showed that the BEs of Fe–O, P–O, and M–OH were denoted by O1s = 530.2, 531.7, and 533.3 eV, respectively; the peak at 533.3 eV was significantly weakened, whereas that at 530.2 eV was enhanced, indicating that hydroxyl and Fe participated in the adsorption process (Yang et al. 2016a; Heitmann et al. 2014).

Table 8 Stoichiometric equivalent between Cd^{2+} and Ca^{2+} in the adsorption process of a 50-mL solution

Initial concentration (mg/L)	0	50	100	200	400	600
Decrease of Cd^{2+} (mmol)	0	0.0206	0.0328	0.0440	0.0501	0.0530
Increase of Ca^{2+} (mmol)	0.0546	0.0662	0.0703	0.0744	0.0838	0.0882

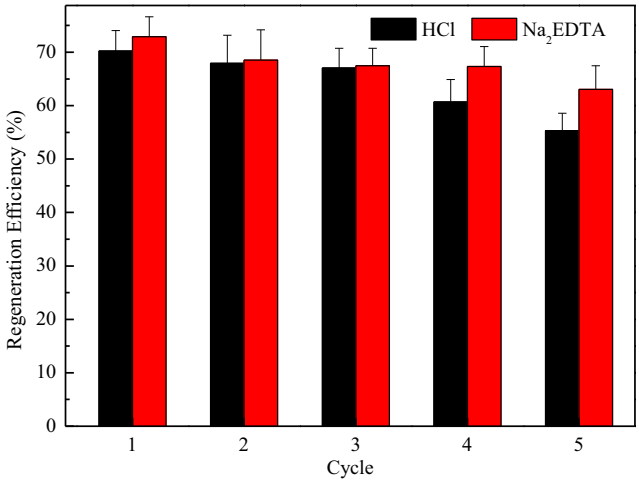

Fig. 11 Regeneration efficiency of nHAP-Fe_3O_4 eluted by HCl and EDTA-Na_2 from batch experiments for five consecutive cycles at 250 mg/L Cd^{2+}

The percentage of Ca^{2+} decreased from 6.8 to 5.9% after adsorption, and the amount of adsorbed Cd^{2+} accounted for 1.6% of the total amount of material, indicating the existence of an ion exchange process. Notably, the percentage of O decreased from 91.9 to 75.9%, and the percentage of P increased from 5.1 to 5.8% because of the reaction of phosphate.

The ion exchange process was explored by measuring the concentration of Ca^{2+} released during the adsorption at initial Cd^{2+} concentrations of 0, 50, 100, 200, 400, and 600 mg/L and a material dosage of 2 g/L. The adsorption data were calculated, as shown in Table 8. The regression analysis showed that the data of the two groups presented highly significant correlation ($P < 0.05$). The release of Ca^{2+} from nHAP-Fe_3O_4 was 0.0546 mmol when the initial concentration of Cd^{2+} was 0 mg/L. Therefore, the ion exchange between Cd^{2+} and Ca^{2+} after subtracting the release of Ca^{2+} from the material was as follows ($R^2 = 0.9382$):

$$y = 0.5828x - 0.0012 \quad (9)$$

where y (mmol) represents the amount of Ca^{2+} which was exchanged by Cd^{2+}, and x (mmol) represents the amount of Cd^{2+} which was adsorbed by nHAP-Fe_3O_4 in a 50-mL solution. The slope of the formula indicated that the amount of Ca^{2+} substituted by per millimolar Cd^{2+} was 0.5828 mmol, indicating that ion exchange occupied an important part of the adsorption process. However, the substitution relationship between Cd^{2+} and Ca^{2+} was not the theoretical 1:1 measurement relationship, indicating the existence of other mechanisms in the adsorption process.

Combining the above results reveals that the adsorption mechanism of Cd^{2+} by nHAP-Fe_3O_4 can be ion exchange and chemical complexation, accompanied by surface physical adsorption. Cd^{2+} diffused to the surface of the adsorbent and then became adsorbed into the active site. The specific surface area of nHAP-Fe_3O_4 had nearly no change after the loading of the nHAP, but the adsorption amount after loading was greatly improved, indicating that surface physical adsorption was not dominant in the adsorption process. The same was true for the influence factors of adsorption.

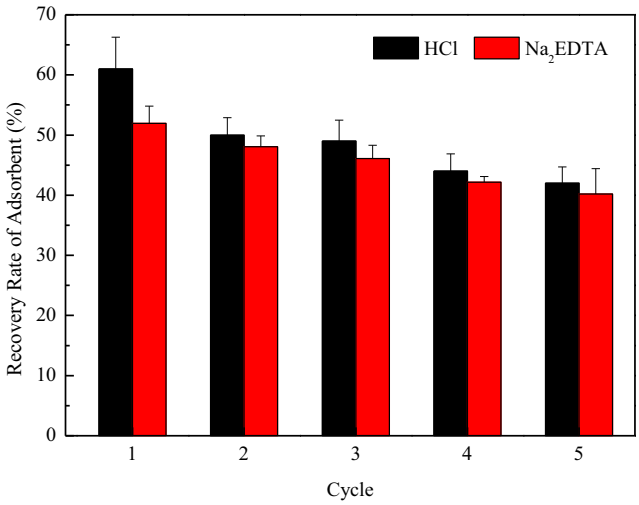

Fig. 12 Recovery rate of nHAP-Fe_3O_4 eluted by HCl and EDTA-Na_2 from batch experiments for five consecutive cycles at 250 mg/L Cd^{2+}

Adsorption–regeneration cycles of Cd^{2+}

As shown in Figs. 11 and 12, the regeneration efficiency and recovery rate of nHAP-Fe_3O_4 decreased with increasing number of cycles. The regeneration efficiencies of nHAP-Fe_3O_4 eluted by HCl after the fifth regeneration cycle and by EDTA-Na_2 were approximately 55.33% and 63.04%, respectively. The recovery rates of the adsorbent eluted by HCl and EDTA-Na_2 were approximately 50% after two cycles. After the fifth cycle, the recovery rates of the adsorbent were 42% and 40.2%. These results suggested that the recovery rate of nHAP-Fe_3O_4 eluted by EDTA-Na_2 was low and that the regeneration efficiency was better than that of HCl. These results may be due to EDTA-Na_2 being a chelating agent with metal ion; hence, it can form a complex with Cd^{2+}, as well as chelates with Fe^{2+} and Fe^{3+}. Hence, the material was dissolved, indirectly causing the Cd^{2+} adsorbed on the material to be desorbed. The regenerations of Cd^{2+} by different adsorbents are shown in Table 9. The desorption of Cd^{2+} adsorbed by nHAP-Fe_3O_4 was lower than that reported probably because the desorption agents, as well as the elements of desorption, were different.

Table 9 Adsorption and regeneration of Cd^{2+} by different adsorbents

No.	Absorbance	Adsorption capacity	Desorption agent	Desorption rate (%)	Ref.
1	FGCX	1.82 mmol/g	0.5 mol/L HCl	97.7	Igberase et al. 2017
2	HANP@AP	250 mg/g	0.05 mol/L HNO_3	> 97.6	Chand and Pakade 2015
3	MNHAP	1.964 mmol/g	0.003 mol/L EDTA	66.2	Yuan et al. 2010
4	PVAf-g-CACTS	51.81	0.1 mol/L HCl	95.6	Meng et al. 2018
5	HAP-Fe_3O_4	62.14 mg/g	0.01 mol/L Na_2EDTA	51.33	This study

Conclusion

HAP-Fe_3O_4 nanocomposite was fabricated by co-precipitation and then compared with Fe_3O_4 nanoparticles. The as-prepared nanocomposite exhibited certain enhancement in material stability. TEM, XRD, FTIR, and magnetic analysis showed that nHAP and Fe_3O_4 were successfully combined and had a good magnetic property for easy separation. The kinetic study showed that the adsorption process achieved equilibrium within 2 h and followed a pseudo-second-order reaction. Adsorption isotherm data fitted the Langmuir model well with an adsorption capacity of 62.14 mg/g. The adsorption mechanisms of Cd^{2+} by nHAP-Fe_3O_4 included rapid surface adsorption, intraparticle diffusion, and internal particle bonding. And the ion exchange of Ca^{2+} and chemical complexation occupied a dominant position. The adsorption amount increased with increasing pH from 2 to 7, and the coexisting ions exhibited great influence on the adsorption capacity, especially Cu^{2+}. HCl and EDTA-Na_2 were efficient eluents used for the desorption of metal ions. After the fifth cycle, the recovery rates of nHAP-Fe_3O_4 were 42% and 40.2%, and the regeneration efficiencies were 55.33% and 63.04%, respectively. These eluents can facilitate the reuse of materials with good regeneration.

Funding information This research was supported by the National Key Research and Development Program of China, project NO.2017YFD0801004.

References

Abollino O, Aceto M, Malandrino M et al (2003) Adsorption of heavy metals on Na-montmorillonite. Effect of pH and organic substances. Water Res 37(7):1619–1627

Adebisi GA, Chowdhury ZZ, Alaba PA (2017) Equilibrium, kinetic, and thermodynamic studies of lead ion and zinc ion adsorption from aqueous solution onto activated carbon prepared from palm oil mill effluent. J Clean Prod 148:958–968

Ahmad ZU, Lian Q, Zappi ME et al (2018) Adsorptive removal of resorcinol on a novel ordered mesoporous carbon (OMC) employing COK-19 silica scaffold: kinetics and equilibrium study. J Environ Sci 75(1):307–317

Ahmad ZU, Yao LG, Wang J et al (2019) Neodymium embedded ordered mesoporous carbon (OMC) for enhanced adsorption of Sunset Yellow: characterizations, adsorption study and adsorption mechanism. Chem Eng J 359:814–826

Ajmal M, Rao RAK, Anwar S et al (2003) Adsorption studies on rice husk: removal and recovery of Cd(II) from wastewater. Bioresour Technol 86(2):147–149

Bachoua H, Renaudin G, Badraoui B et al (2016) Preparation and characterization of functionalized hybrid hydroxyapatite from phosphorite and its potential application to Pb^{2+} remediation. J Sol-Gel Sci Technol 78(3):621–631

Basualto C, González P, Briso A et al (2017) Synthesis and use of nanomagnetic MnO_2 adsorbent for removing Pb(II) and Cd(II) ions from acid aqueous solutions. Desalin Water Treat 70:175–182

Beesley L, Marmiroli M (2011) The immobilisation and retention of soluble arsenic, cadmium and zinc by biochar. Environ Pollut 159(2):474–480

Chand P, Pakade YB (2015) Synthesis and characterization of hydroxyapatite nanoparticles impregnated on apple pomace to enhanced adsorption of Pb(II), Cd(II), and Ni(II) ions from aqueous solution. Environ Sci Pollut Res Int 22(14):10919–10929

Chen M, Wu P, Yu L et al (2017) FeOOH-loaded MnO_2 nano-composite: an efficient emergency material for thallium pollution incident. J Environ Manag 192:31–38

Cheng C, Wang J, Yang X et al (2014) Adsorption of Ni(II) and Cd(II) from water by novel chelating sponge and the effect of Alkali-Earth metal ions on the adsorption. J Hazard Mater 264(2):332–341

Dey P, Gola D, Mishra A et al (2016) Comparative performance evaluation of multi-metal resistant fungal strains for simultaneous removal of multiple hazardous metals. J Hazard Mater 318:679–685

Farokhi M, Parvareh A, Moraveji MK (2018) Performance of ceria/iron oxide nano-composites based on chitosan as an effective adsorbent for removal of Cr(VI) and Co(II) ions from aqueous systems. Environ Sci Pollut Res 25:27059–27073

Guivar JAR, Sanches EA, Bruns F et al (2016) Vacancy ordered γ-Fe_2O_3 nanoparticles functionalized with nanohydroxyapatite: XRD, FTIR, TEM, XPS and Mössbauer studies. Appl Surf Sci 389:721–734

Guo J, Han Y, Mao Y et al (2017) Influence of alginate fixation on the adsorption capacity of hydroxyapatite nanocrystals to Cu^{2+} ions. Colloids Surf A Physicochem Eng Asp 529:801–807

Guo L, Li Z, Xu L et al (2018) The dynamics and adsorption of Cd (II) onto hydroxyapatite attapulgite composites from aqueous solution. J Sol-Gel Sci Technol 87:269–284

Heitmann AP, Silva GC, Paiva PRP et al (2014) Synthesis and characterization of a magnetic nanostructured composite containing manganese oxide for removal of Cd(II) from aqueous medium. Ceramica 60(355):429–435

Igberase E, Osifo P, Ofomaja A (2017) The adsorption of Pb, Zn, Cu, Ni, and Cd by modified ligand in a single component aqueous solution: equilibrium, kinetic, thermodynamic, and desorption studies. Int J Anal Chem 2017:1–15

Karami H (2013) Heavy metal removal from water by magnetite nanorods. Chem Eng J 219(3):209–216

Ke S, Cheng XY, Zhang JY et al (2015) Estimation of the benchmark dose of urinary cadmium as the reference level for renal dysfunction: a large sample study in five cadmium polluted areas in China. BMC Public Health 15(1):656

Khraisheh MAM, Al-Degs YS, Mcminn WAM (2004) Remediation of wastewater containing heavy metals using raw and modified diatomite. Chem Eng J 99(2):177–184

Langmuir I (1918) The adsorption of gases on plane surfaces of glass, mica and platinum. J Am Chem Soc 40(9):1361–1403

Lee SY, Choi HJ (2018) Persimmon leaf bio-waste for adsorptive removal of heavy metals from aqueous solution. J Environ Manag 209:382–392

Lei L, Wang F, Lv Y et al (2018) Halloysite nanotubes and Fe_3O_4 nanoparticles enhanced adsorption removal of heavy metal using electrospun membranes. Appl Clay Sci 161:225–234

Liang Y, Cao X, Zhao L et al (2014) Biochar- and phosphate-induced immobilization of heavy metals in contaminated soil and water: implication on simultaneous remediation of contaminated soil and groundwater. Environ Sci Pollut Res Int 21(6):4665–4674

Liang J, Liu M, Zhang Y (2016) Cd(II) removal on surface-modified activated carbon: equilibrium, kinetics and mechanism. Water Sci Technol 74(8):1800–1808

Ling LL, Liu WJ, Zhang S et al (2017) Magnesium oxide embedded nitrogen self-doped biochar composites: fast and high-efficiency adsorption of heavy metals in an aqueous solution. Environ Sci Technol 51(17):10081–10089

Liu JF, Zhao ZS, Jiang GB (2015) Coating Fe_3O_4 magnetic nanoparticles with humic acid for high efficient removal of heavy metals in water. Environ Sci Technol 42(18):6949–6954

Ma Z, Guan Y, Liu H (2005) Synthesis and characterization of micron-sized monodisperse superparamagnetic polymer particles with amino groups. J Polym Sci A Polym Chem 43(15):3433–3439

Ma H, Pu S, Hou Y et al (2018a) A highly efficient magnetic chitosan "fluid" adsorbent with a high capacity & fast adsorption kinetics for dyeing wastewater purification. Chem Eng J 345:556–565

Ma J, Xue F, Jiang L et al (2018b) Magnetic flocculants synthesized by Fe_3O_4 coated with cationic polyacrylamide for high turbid water flocculation. Environ Sci Pollut Res 25:25955–25966

Meng J, Cui J, Yu J et al (2018) Preparation of green chelating fibers and adsorption properties for Cd(II) in aqueous solution. J Mater Sci 53(3):1–13

Nabavinia M, Khoshfetrat AB, Naderi-Meshkin H (2019) Nano-hydroxyapatite-alginate-gelatin microcapsule as a potential osteogenic building block for modular bone tissue engineering. Mater Sci Eng C Mater Biol Appl 97:67–77

Núñez JD, Benito AM, González R et al (2014) Integration and bioactivity of hydroxyapatite grown on carbon nanotubes and graphene oxide. Carbon 79(1):590–604

Piar C, Pakade YB (2015) Synthesis and characterization of hydroxyapatite nanoparticles impregnated on apple pomace to enhanced adsorption of Pb(II), Cd(II), and Ni(II) ions from aqueous solution. Environ Sci Pollut Res 22(14):10919–10929

Qian M (2007) Advances in new technology for heavy metal wastewater treatment at home and abroad. Chin J Chem Eng 1(7):10–14

Rahmanian O, Dinari M, Abdolmaleki MK (2018) Carbon quantum dots/layered double hydroxide hybrid for fast and efficient decontamination of Cd(II): the adsorption kinetics and isotherms. Appl Surf Sci 428:272–279

Schiewer S, Patil SB (2008) Pectin-rich fruit wastes as biosorbents for heavy metal removal: equilibrium and kinetics. Bioresour Technol 99(6):1896–1903

Shan RR, Yan LG, Yang K et al (2015) Adsorption of Cd(II) by Mg-Al-CO_3- and magnetic Fe_3O_4/Mg-Al-CO_3-layered double hydroxides: kinetic, isothermal, thermodynamic and mechanistic studies. J Hazard Mater 299(9):42–49

Son EB, Poo KM, Chang JS et al (2018) Heavy metal removal from aqueous solutions using engineered magnetic biochars derived from waste marine macro-algal biomass. Sci Total Environ 615:161–168

Su Y, Adeleye AS, Huang Y et al (2014) Simultaneous removal of cadmium and nitrate in aqueous media by nanoscale zerovalent iron (nZVI) and Au doped nZVI particles. Water Res 63(7):102–111

Tang N, Niu CG, Li XT (2018) Efficient removal of Cd and Pb from aqueous solution with amino- and thiol-functionalized activated carbon isotherm and kinetics modeling. Sci Total Environ 635:1331–1344

Viswanathan N, Meenakshi S (2008) Enhanced fluoride sorption using La(III) incorporated carboxylated chitosan beads. J Colloid Interface Sci 322(2):375–383

Wan S, Bing C, Ahmad ZU et al (2016) Ordered mesoporous carbon preparation by the in situ radical polymerization of acrylamide and its application for resorcinol removal. J Appl Polym Sci 133(19):1–11

Wei N, Cheng P, Zhou X et al (2017) Three-dimensional porous scaffold by self-assembly of reduced graphene oxide and nano-hydroxyapatite composites for bone tissue engineering. Carbon 116(Complete):325–337

Wu J, Huang D, Liu X et al (2018) Remediation of As(III) and Cd(II) co-contamination and its mechanism in aqueous systems by a novel calcium-based magnetic biochar. J Hazard Mater 348:10–19

Yamamura H, Da SV, Plm R et al (2018) Physico-chemical characterization and biocompatibility of hydroxyapatite derived from fish waste. J Mech Behav Biomed Mater 80:137–142

Yang L, Wei Z, Zhong W et al (2016a) Modifying hydroxyapatite nanoparticles with humic acid for highly efficient removal of Cu(II) from aqueous solution. Colloids Surf A Physicochem Eng Asp 490:9–21

Yang L, Zhong W, Cui J et al (2016b) Enhanced removal of Cu(II) ions from aqueous solution by poorly crystalline hydroxyapatite nanoparticles. J Dispers Sci Technol 37:956–968

Yuan F, Gong JL, Zeng GM et al (2010) Adsorption of Cd(II) and Zn(II) from aqueous solutions using magnetic hydroxyapatite nanoparticles as Aadsorbents. Chem Eng J 162(2):487–494

Zendehdel M, Ramezani M, Shoshtariyeganeh B et al (2018) Simultaneous removal of Pb(II), Cd(II) and bacteria from aqueous solution using amino-functionalized Fe_3O_4/NaP zeolite nanocomposite. Environ Technol 18:1–16

Zhang C, Shan B, Tang W et al (2017) Comparison of cadmium and lead sorption by phyllostachys pubescens biochar produced under a low-oxygen pyrolysis atmosphere. Bioresour Technol 238:352–360

Zhang X, Sun C, Zhang L et al (2018a) Adsorption studies of cadmium onto magnetic Fe_3O_4@$FePO_4$ and its preconcentration with detection by electrothermal atomic absorption spectrometry. Talanta 181:352–358

Zhang Z, Wang X, Hao W et al (2018b) Removal of Pb(II) from aqueous solution using hydroxyapatite/calcium silicate hydrate (HAP/C-S-H) composite adsorbent prepared by a phosphate recovery process. Chem Eng J 344:53–61

Zheng LC, Dang Z, Yi XY et al (2010) Equilibrium and kinetic studies of adsorption of Cd(II) from aqueous solution using modified corn stalk. J Hazard Mater 176(1-3):650–656

Zhou Q, Liao B, Lin L et al (2017) Adsorption of Cu(II) and Cd(II) from aqueous solutions by ferromanganese binary oxide–biochar composites. Sci Total Environ 615:115–122

Zhou H, Jiang Z, Wei S et al (2018) Adsorption of Cd(II) from aqueous solutions by a novel layered double hydroxide FeMnMg-LDH. Water Air Soil Pollut 229(3):78

Zhuzhou (2007) Preparation and characterization of magnetite Fe_3O_4 nanopowders. Rare Metal Mater Eng 36(6):238–243